



Elemental mercury (Hg^0) removal over spinel LiMn_2O_4 from coal-fired flue gas

Haomiao Xu ^a, Hongbo Zhang ^{a,b}, Songjian Zhao ^{a,c}, Wenjun Huang ^a, Zan Qu ^a, Naiqiang Yan ^{a,*}

^aSchool of Environmental Science and Engineering, Shanghai Jiao Tong University, Shanghai 200240, China

^bSchool of Materials Science and Engineering, Shanghai Jiao Tong University, Shanghai 200240, China

^cSchool of Chemistry and Chemical Engineering, Shanghai Jiao Tong University, Shanghai 200240, China

HIGHLIGHTS

- Spinel LiMn_2O_4 was used as heterogeneous catalyst.
- LiMn_2O_4 had higher Hg^0 removal efficiency than Mn_2O_3 and $\text{Li}_2\text{O}-\text{Mn}_2\text{O}_3$.
- The mechanisms for Hg^0 removal over spinel LiMn_2O_4 were discussed.

ARTICLE INFO

Article history:

Received 17 February 2016

Received in revised form 18 April 2016

Accepted 19 April 2016

Available online 22 April 2016

Keywords:

Elemental mercury

Manganese oxides

Lithium

Spinel oxide

ABSTRACT

Spinel LiMn_2O_4 was prepared using a sol–gel method to investigate gaseous elemental mercury (Hg^0) removal performance from coal-fired power plants. The physical and chemical characterization results indicated that LiMn_2O_4 had a basic MnO_6 unit and Li ions in the spinel $\lambda\text{-MnO}_2$ structure. LiMn_2O_4 exhibited better Hg^0 removal performance than that of pure Mn_2O_3 and mixed oxides of $\text{Li}_2\text{O}-\text{Mn}_2\text{O}_3$. Hg^0 removal efficiency of LiMn_2O_4 was 93.09% (600 min reaction) at an optimum temperature of 150 °C. Higher temperature (>200 °C) was not favorable for Hg^0 removal. O_2 enhanced the Hg^0 removal efficiency of LiMn_2O_4 , while SO_2 and H_2O inhibited the reaction, and the co-existence of them had a poison effect on Hg^0 removal. The primary Hg^0 removal mechanism was chemical-adsorption, Hg^0 was firstly catalytic oxidized to Hg^{2+} along with the reduction of high valance of Mn ($\text{Mn}^{4+}/\text{Mn}^{3+}$) to low valance ($\text{Mn}^{3+}/\text{Mn}^{2+}$). Hg^{2+} was combined with adsorbed oxygen and existed as $\text{Hg}-\text{O}$ on LiMn_2O_4 surface. The existence of Li ions constructs a $\lambda\text{-MnO}_2$ structure and benefits the oxidation process. Furthermore, based on the Hg -TPD results, the desorption activation energy was 58.82 kJ/mol.

© 2016 Elsevier B.V. All rights reserved.

1. Introduction

Elemental mercury (Hg^0) emitted from coal-fired power plants is hazardous in the atmosphere [1]. Up to now, many approaches had been developed to control the emission of Hg^0 [2–6]. According to the Hg^0 removal mechanism, it can be classified to two Hg^0 control methods: (1) catalytic oxidation of Hg^0 to oxidized mercury (Hg^{2+}) and (2) adsorption of Hg^0 by sorbents. Although the Hg^{2+} in the flue gas can be removed by wet flue gas desulfurization (WFGD) devices, mercury enriched in the slurry could cause mercury secondary contamination [7]. However, the adsorption of Hg^0 on the sorbents was not stable by physical-adsorption [8]. Enhancement of catalytic oxidation of Hg^0 to Hg^{2+} , followed by

chemical-adsorption was a potential method for the efficient mercury control.

Among various Hg^0 catalysts or sorbents, manganese-based oxides (MnO_x) were potential materials due to their higher redox potential, low cost and environmental friendliness. Bulk metal oxides have long been an interest as heterogeneous catalytic oxidation catalysts. To enhance Hg^0 removal performances of MnO_x , lots of manganese-based oxides have been developed and evaluated in the laboratory. Ce– MnO_x [9,10], Sn– MnO_x [11], Fe– MnO_x [11,12] and other binary metal oxides were synthesized to enlarge Hg^0 adsorption capacities, to enlarge reaction temperature window and to enhance SO_2 resistance performance, etc. It was accepted that the Hg^0 removal mechanism can be described as follows: Hg^0 first adsorbed on the surface of MnO_x , followed the catalytic oxidation by high valance of Mn ($\text{Mn}^{4+}/\text{Mn}^{3+}$), after that the oxidized mercury combined with adsorbed oxygen to form $\text{Hg}-\text{O}$ species. The primary Hg^0 removal process was ascribed to a

* Corresponding author. Tel./fax: +86 21 54745591.

E-mail address: nqyan@sjtu.edu.cn (N. Yan).

chemical-adsorption process. During this process, the higher surface area, sufficient adsorbed oxygen and higher valance state of Mn are beneficial for Hg⁰ removal.

MnO_x occur naturally as minerals in at least 30 different crystal structures. Our recent studies found that the crystal structures of MnO₂ significantly affects Hg⁰ catalytic oxidation and adsorption [13]. The Hg⁰ removal performance over α-, β- and γ-MnO₂ has an order of α-MnO₂ > γ-MnO₂ ≥ β-MnO₂. It has been acknowledged that high crystallinity would increase the stability and enhance the catalytic performance. Mn-based perovskite oxides have indicated to have high gas-phase heterogeneous catalytic oxidation performance [14,15]. Moreover, among Mn-based perovskite oxides, LaMnO₃ had superior catalytic removal performance for Hg⁰ [16,17]. The effects of crystal structure of manganese oxides on the catalysis activity showed be further developed.

Spinel LiMn₂O₄ was an interesting cathode material for lithium-ion batteries due to its low cost, low toxicity and high voltage [18]. LiMn₂O₄ exhibited three-dimensional frameworks, comprising MnO₆ octahedral units and coexisting Li ions. In general, Li ions can be fully extracted from the spinel framework of LiMn₂O₄ to produce a spinel-type λ-MnO₂ that LiMn₂O₄ often acted as Li⁺ ion selective adsorbent. And it has been reported that LiMn₂O₄ had a water oxidation performance because the role of λ-MnO₂ [19,20]. However, to our knowledge, there were still no reports about using spinel LiMn₂O₄ for the gas-phase heterogeneous catalytic oxidation.

In this study, LiMn₂O₄ was synthesized to investigate the Hg⁰ removal performance. The BET, XRD, Raman, H₂-TPR and XPS were employed for the chemical and physical characterization. The Hg⁰ removal performance was evaluated in a fixed-bed adsorption system. The effects of gas components and the mechanism for Hg⁰ removal was discussed. Furthermore, the mercury release performance was evaluated and the desorption energy was calculated.

2. Experimental section

2.1. Materials preparation

LiMn₂O₄ was synthesized according to the citrate complexation procedure. Stoichiometric amounts of the metallic nitrates (LiNO₃ and Mn(NO₃)₃) were firstly dissolved in the distilled water. Thereafter, an aqueous solution of citric acid (CA), was slowly added to the precursor solution under gentle stirring. The molar ratio of Li:Mn:CA was 1:1:2. Solvent evaporation was performed at 80 °C until the formation of gel. After vigorous stirring and evaporation, a transparent gel was formed, which was dried at 100 °C overnight. The obtained precursor was calcined at 300 °C for 1 h in air to completely decompose citric acid followed by calcination at 500 °C for 5 h at a rate of 10 °C/min. Mn₂O₃ and Li₂O were also synthesized according to the same sol-gel method. Additionally, the physical mixed oxides of Li₂O–Mn₂O₃ were synthesized for comparison.

2.2. Materials characterization

X-ray diffraction (XRD) was carried out using X-ray diffractometer equipped with a Cu–Kα radiation (APLX-DUO, BRUKER, Germany). Diffractograms were collected in the 2θ range from 10° to 80° with a scanning velocity of 5°/min. Raman spectroscopy was used for the determination of the crystallinity degree of the materials. The analyses were performed in a SENTERRA R200 microscope. The 633 nm line of Ar⁺ laser was used for the excitation. The multipoint Brunauer–Emmett–Teller (BET) surface areas and pore analysis were performed using a N₂ sorption measurement (Nova-2200e) at 77 K. The pore size and pore volume were

calculated based on the Barrett–Joyner–Halenda (BJH) method. X-ray photoelectron spectroscopy (XPS) was used to analyze the surface characteristics of as-prepared materials. The XPS system contained an AXIS Ultra DLD (Shimadzu–Kratos) spectrometer with Al–Kα as the excitation source. The C 1 s line at 284.6 eV was taken as a reference for the binding energy calibration. The reducibility of the samples was determined using H₂-TPR experiments, and these experiments were performed on a Chemisorp TPx 290 instrument. The samples were degassed at 200 °C for 3 h under an Ar atmosphere prior to the tests, and the reducing gas consisted of 10% H₂/Ar.

A mercury-temperature programmed desorption (Hg-TPD) method was employed to investigate the regeneration characteristics of the as-prepared materials. After mercury adsorption at 150 °C with 4% O₂ for 30 min, the sorbents were regenerated by heating from 100 to 700 °C in a pure N₂ carrier gas. Hg-TPD curves under different heating rates (2 °C/min, 5 °C/min and 10 °C/min) on the LiMn₂O₄ surfaces were collected. The desorption activation energy was also calculated according to the results.

2.3. Hg⁰ fix-bed adsorption

A lab-scale fixed-bed adsorption system was assembled, as shown in Fig. 1, to explore the uptake capacity of Hg⁰ by the as-prepared materials. The experimental method was similar to our previous studies [21]. The fixed-bed reactor was constructed to allow for a total gas flow of 500 ml/min. Temperature control devices were installed to control the mixed gas and the reactor temperature. The reaction temperatures range from 100 to 300 °C. 20 mg of as-prepared materials were used for each experiment and it was put in a quartz tube with a diameter of 4 cm. During the Hg⁰ removal experiments, the mercury inlet gas bypassed the as-prepared material and then passed into the analytical system until the desired inlet mercury concentration was established. The mercury analyzer was CVASS in this study. Before each test, the Hg⁰ concentration was adjusted by Lumex RA 915. In addition, active carbon was used for the off-gas cleaning. It can adsorb the mercury (Hg²⁺ and Hg⁰) in the flue gas. KMnO₄ was used for adsorbed the oxidized mercury.

To investigate the effect of temperature on the flue gas, the area under the breakthrough curves corresponding to Hg⁰ on the prepared sorbents during the test time was integrated. To investigate the effects of various gas components, 4% O₂, 500 ppm SO₂ and 4% H₂O were chosen when needed. These gases were firstly get through a mixed gas tank.

The Hg⁰ removal efficiency was calculated according to Eq. (1):

在此处键入公式。

$$x_{\text{Hg}} = \frac{-b \pm \sqrt{b^2 - 4ac}}{2a}$$

$$\text{Hg}^0 \text{ removal efficiency} = \frac{\text{Hg}_{\text{in}}^0 - \text{Hg}_{\text{out}}^0}{\text{Hg}_{\text{in}}^0} \quad (1)$$

where Hg_{in}⁰ was the inlet concentration of Hg⁰, and Hg_{out}⁰ was the outlet concentration of Hg⁰.

3. Results and discussion

3.1. Physicochemical properties

Fig. 2 presented X-ray diffraction (XRD) patterns of the as-prepared samples. The XRD patterns of Li₂O, Mn₂O₃, LiMn₂O₄ and Li₂O–Mn₂O₃ samples was collected. For Li₂O, it existed in an amorphous phase. The peaks in the pure manganese oxide was ascribed

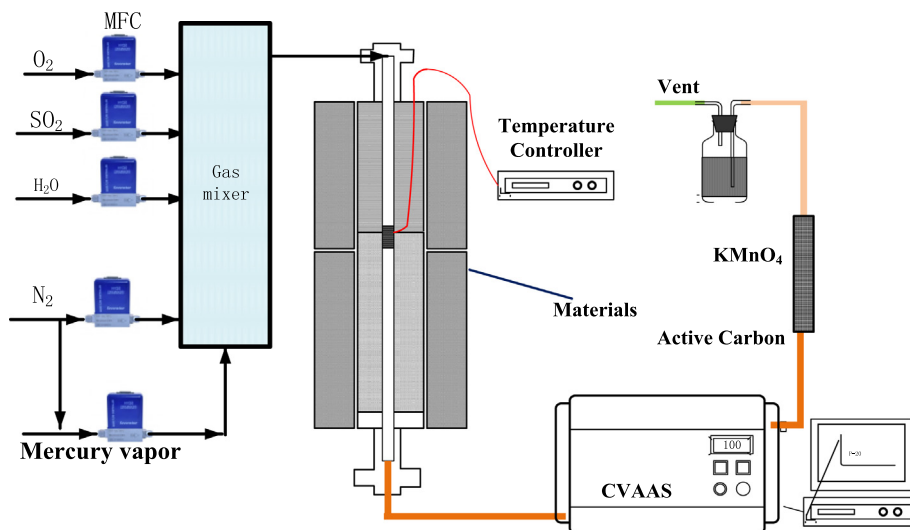


Fig. 1. Process flow diagram for mercury removal assessment.

to Mn_2O_3 in accordance with PDF card of No. 24-0508. For LiMn_2O_4 , the peaks at 18° , 35° , 43° , 58° , 63° and 67° were well-defined structure in good agreement with spinel LiMn_2O_4 with PDF card of No. 35-0782 [22]. There were no other phases in the patterns of LiMn_2O_4 . It indicated that the spinel LiMn_2O_4 was successfully synthesized. For comparison, the XRD pattern of $\text{Li}_2\text{O}-\text{Mn}_2\text{O}_3$ mixed oxide was collected. Interestingly, $\text{Li}_2\text{O}-\text{Mn}_2\text{O}_3$ has mixed phases of Mn_2O_3 and spinel LiMn_2O_4 . There were no patterns can be ascribed to Li_2O . It could be speculated that the flexible Li^+ ions could enter into manganese oxide to form LiMn_2O_4 , and residual Mn_2O_3 still remain its own crystal phase.

To further investigate the structural features of as-prepared samples, Raman spectra was employed and the results are shown in Fig. 3. In the spinel LiMn_2O_4 , it had a wide peak centered at 641 cm^{-1} , it was the characteristic of vibrations involving motion of oxygen atoms inside the octahedral MnO_6 unit. The basic structure of manganese oxides was MnO_6 octahedral unit, and that the Raman shift was at about $600\text{--}700\text{ cm}^{-1}$ [23,24]. The vibrations were detected at 689 and 615 cm^{-1} for Mn_2O_3 and $\text{Li}_2\text{O}-\text{Mn}_2\text{O}_3$, respectively. However, the intensity of LiMn_2O_4 was stronger than that of Mn_2O_3 and $\text{Li}_2\text{O}-\text{Mn}_2\text{O}_3$, which indicated a better

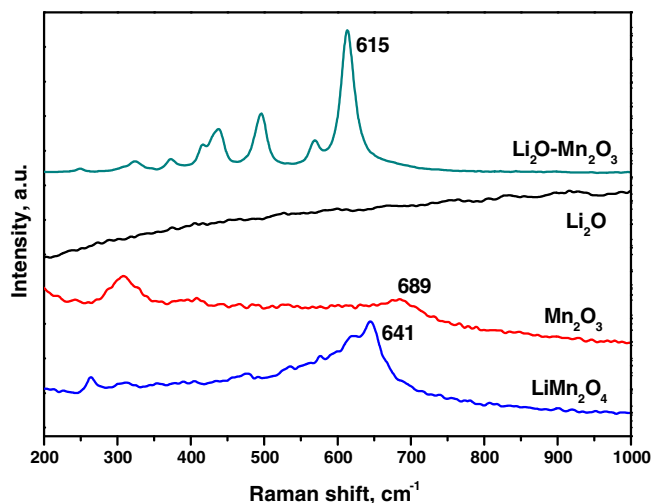


Fig. 3. Raman spectra of as-prepared samples.

crystallization. The bands of LiMn_2O_4 and $\text{Li}_2\text{O}-\text{Mn}_2\text{O}_3$ broadened and down-shifted when the particles became smaller. For instance, the distinct features at 689 cm^{-1} for bulk Mn_2O_3 shifted to 641 cm^{-1} for LiMn_2O_4 , accompanied by broadening of the bands. The formation of $\text{Li}_2\text{O}-\text{Mn}_2\text{O}_3$ had smaller particle size than LiMn_2O_4 .

As presented in Table 1, the BET surface areas and pore properties of the as-prepared materials were analyzed. Mn_2O_3 had a small BET surface area of $11.2\text{ m}^2/\text{g}$. It is smaller than that of Li_2O ($40.1\text{ m}^2/\text{g}$). For LiMn_2O_4 , the BET surface area ($41.2\text{ m}^2/\text{g}$) which was much larger than that of Mn_2O_3 . The pore size of LiMn_2O_4 and Mn_2O_3 were 3.618 and 3.825 nm , respectively. However, the pore volume of LiMn_2O_4 was three times larger than that of Mn_2O_3 . The sufficient pores in LiMn_2O_4 resulted in the higher surface area. In addition, $\text{Li}_2\text{O}-\text{Mn}_2\text{O}_3$ had the largest BET surface area ($53.2\text{ m}^2/\text{g}$) among the as-prepared samples. The physical mixed oxides had large pore volume which was $0.812\text{ m}^3/\text{g}$. After Li^+ ions entered into the basic octahedral MnO_6 unit, the surface area of prepared Mn-based material was enlarged.

The chemical compositions of LiMn_2O_4 were analyzed by X-ray photoelectron spectra (XPS). As XPS spectra shown in Fig. 4(a), in the region of O 1s, Li_2O had only one peak at 531.3 eV , the high

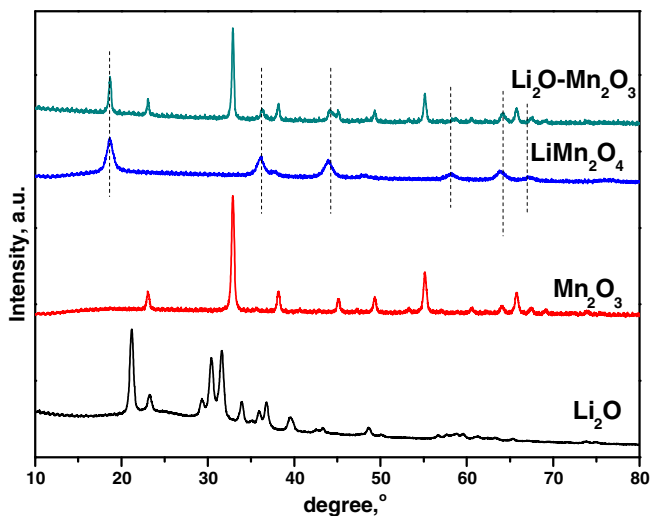


Fig. 2. XRD patterns of as-prepared samples.

Table 1
BET surface area, BJH pore properties and XPS analysis of as-prepared materials.

Materials	BET surface area (m ² /g)	Pore volume (m ³ /g)	Pore size (nm)	O (%)		Mn (%)	
				O _{ads}	O _{latt}	Mn ⁴⁺	Mn ³⁺
Li ₂ O	40.1	0.073	3.825	100	–	–	–
Mn ₂ O ₃	11.2	0.051	3.301	44.24	55.76	–	100
LiMn ₂ O ₄	41.2	0.154	3.618	39.32	60.68	21.88	78.12
Li ₂ O–Mn ₂ O ₃	53.2	0.812	3.646	55.92	44.08	–	100

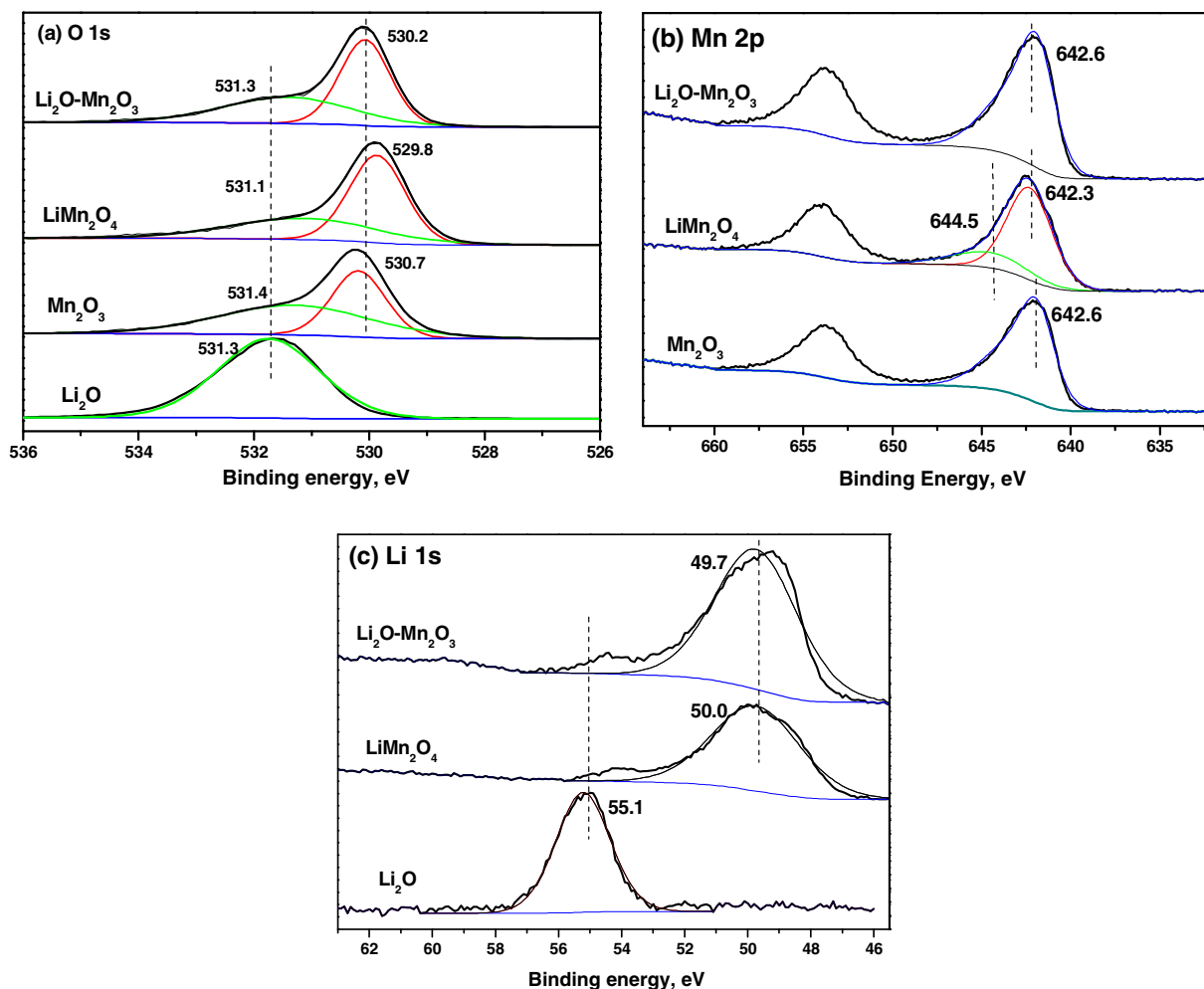


Fig. 4. XPS profiles for LiMn₂O₄, Mn₂O₃, Li₂O and Li₂O–Mn₂O₃.

binding energy of such oxygen indicated the instability of Li₂O. For Mn₂O₃, two peaks at 531.4 and 530.7 eV were corresponded to the surface adsorbed oxygen (O_{ads}) and lattice oxygen (O_{latt}), respectively [21]. Similarly, LiMn₂O₄ and Li₂O–Mn₂O₃ had these two character peaks which can be ascribed to O_{ads} and O_{latt}. However, the ratio of O_{ads}/O_{latt} was quite a different. From the results listed in Table 1, the ratio of O_{ads}/O_{latt} for Mn₂O₃ and LiMn₂O₄ were 44.24/55.76 and 39.32/60.68, respectively. Li₂O–Mn₂O₃ had the highest ratio of 55.92/45.08. It had been proven that O_{ads} was the adsorption site for the oxidized mercury. The higher concentration of surface adsorbed oxygen was due to the mobility of Li ions. Li ions entered into Mn₂O₃ and formed spinel LiMn₂O₄, resulted in the residual oxygen on its surface.

As shown in Fig. 4(b), in the spectra of Mn 2p, for LiMn₂O₄, the peaks at 644.5 and 642.3 eV were corresponded to Mn⁴⁺ and Mn³⁺, respectively. The ratio of Mn⁴⁺/Mn³⁺ was 21.88/78.12. for

Mn₂O₃, the peaks detected at 642.6 eV was ascribed to Mn³⁺. Li₂O–Mn₂O₃ had one peak at 642.6 eV and it was ascribed to Mn³⁺. The spinel LiMn₂O₄ had higher valence of Mn which was due to the unstable of Li⁺ in LiMn₂O₄. Generally, with the addition of Li ions in the manganese oxides, the reaction of “2Mn³⁺ = – Mn⁴⁺ + Mn²⁺” occurred. Therefore, the binding energy of Mn³⁺ for LiMn₂O₄ was lower than that of Mn₂O₃. Li ions ascend the valance of Mn in LiMn₂O₄ which was beneficial for catalytic oxidation.

In the region of Li 1 s, as shown in Fig. 4(c), for Li₂O, the line has a binding energy centered at 55.1 eV, the low binding energy indicated that Li has low electron binding capacity. But for LiMn₂O₄ and Li₂O–Mn₂O₃, they presented two peaks on their spectra. One small peak at 55.1 eV and another primary peak at approximately 50.0 eV. The co-existence of Li and Mn resulted in the higher mobility of Li ions in the spinel LiMn₂O₄ structure.

Based on the above discussion, LiMn_2O_4 was synthesized using simple sol–gel method, it existed a basic spinel structure. With the addition of Li ions in the Mn-base structure, the surface area was enlarged and the valance of Mn was increased.

3.2. Hg^0 removal performances over LiMn_2O_4

3.2.1. Hg^0 removal efficiencies over as-prepared samples

The Hg^0 removal performances over the as-prepared materials were tested, and the results are shown in Fig. 5. Obviously, Li_2O had nearly no activity for Hg^0 . Mn_2O_3 had 90% Hg^0 removal efficiency in the initial 100 min. But it gradually lost its activity for Hg^0 , it had only approximately 23% Hg^0 removal efficiency after 600 min reaction. For LiMn_2O_4 , it presented excellent performance for Hg^0 removal, the Hg^0 removal efficiency was higher than 99% even after 600 min reaction. LiMn_2O_4 showed quite a different performance compared to that of Mn_2O_3 . In order to further identify the effect of crystal structure, the performance of the mixed oxide ($\text{Li}_2\text{O}-\text{Mn}_2\text{O}_3$) was investigated. The Hg^0 removal performance was not as well as LiMn_2O_4 , even was worse than Mn_2O_3 . The Hg^0 removal efficiency drop rapidly, and the Hg^0 removal efficiency was only approximately 30% after 600 min reaction. As discussed above, the mixed oxide of $\text{Li}_2\text{O}-\text{Mn}_2\text{O}_3$ had largest surface area among the as-tested materials, and it had a mixed phase of Mn_2O_3 and spinel LiMn_2O_4 . However, it didn't showed a better performance for Hg^0 removal. The bulk partiles of $\text{Li}_2\text{O}-\text{Mn}_2\text{O}_3$ resulted in the larger pore volume and surface area. However, the primary Mn active sites was occupied and the catalytic effect of LiMn_2O_4 can't exhibit. The results confirmed that spinel LiMn_2O_4 was favorable for Hg^0 removal.

3.2.2. Effect of temperature on Hg^0 removal efficiencies over LiMn_2O_4

The effect of reaction temperature on Hg^0 removal efficiencies over LiMn_2O_4 were investigated at a wide reaction temperature window (100–300 °C). For comparison, the performances of Mn_2O_3 and $\text{Li}_2\text{O}-\text{Mn}_2\text{O}_3$ were also investigated. The Hg^0 removal efficiencies were calculated based on the total 600 min reaction. As shown in Fig. 6, LiMn_2O_4 had higher than 90% removal efficiencies at 100 and 150 °C, and the highest removal efficiency was 93.09% at 150 °C. However, the Hg^0 removal efficiencies decreased sharply as the reaction temperature increased to 200 °C, it had only 52.4% Hg^0 removal efficiency. As the temperature rising, the Hg^0 removal efficiencies further decreased. For Mn_2O_3 , the highest Hg^0 removal efficiency was 80.1% at 100 °C. The Hg^0 removal effi-

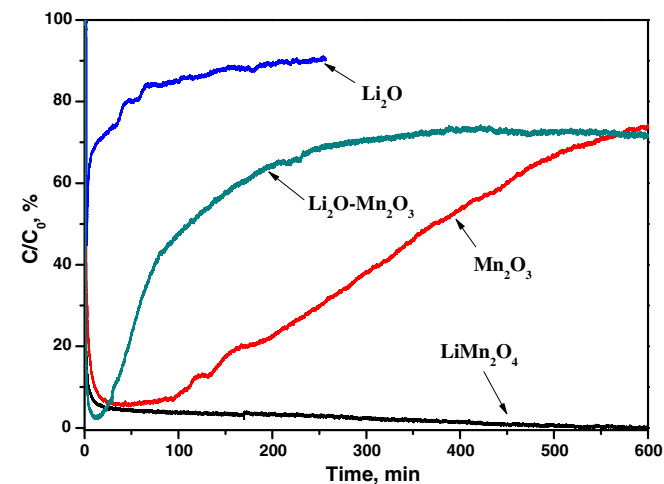


Fig. 5. Hg^0 removal efficiencies over different materials.

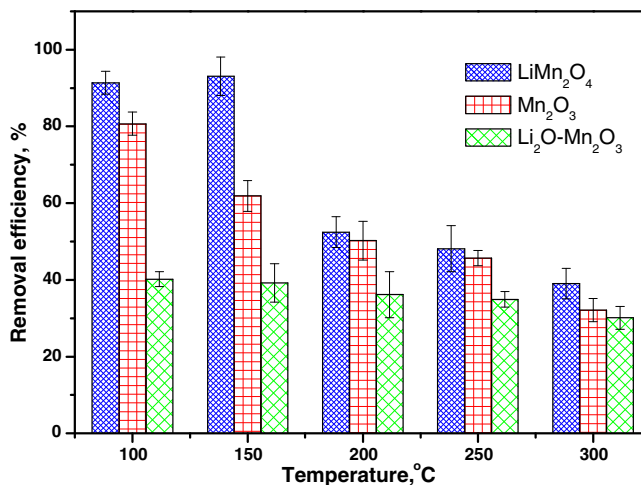


Fig. 6. Effect of temperature on Hg^0 removal efficiencies.

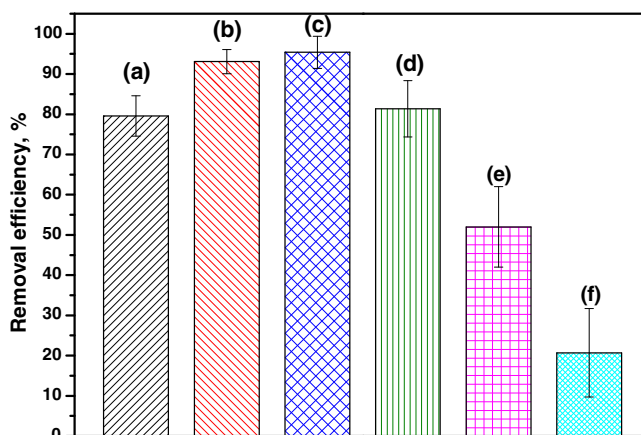


Fig. 7. Effect of O_2 , SO_2 and H_2O on Hg^0 removal efficiencies. (b) N_2 , (b) 4% O_2 , (c) 8% O_2 , (d) 500 ppm SO_2 + 4% O_2 , (e) 4% H_2O + 4% O_2 and (f) 500 ppm SO_2 + 4% H_2O + 4% O_2 .

ciency decreased sharply as the temperature increased, and it had only approximately 32% Hg^0 removal efficiency when the temperature was 300 °C. The mixed oxide $\text{Li}_2\text{O}-\text{Mn}_2\text{O}_3$ had approximately 40% Hg^0 removal efficiencies at 100–150 °C. And the Hg^0 removal efficiencies were decreased as the temperature rising. Obviously, as-prepared Mn-based material lost their activities when the temperature was higher than 200 °C, LiMn_2O_4 had the best performance at 150 °C. The material can be used downstream of the electrostatic precipitator/fan filter (ESP/FF) units in a coal-fired power plant.

3.2.3. Effect of O_2 , SO_2 and H_2O on Hg^0 removal efficiencies over LiMn_2O_4

Furthermore, the effects of gas components on Hg^0 removal efficiencies over LiMn_2O_4 were investigated and the results are presented in Fig. 7. In the absence of O_2 , Hg^0 removal efficiency was 79.1%, which is the average removal efficiency of total 600 min. When the simulated gas had 4% O_2 , the Hg^0 removal performance was enhanced, the calculated Hg^0 removal efficiency was 93.09%. To further investigate the effect of O_2 on Hg^0 removal, 8% O_2 was added in the simulated gas, the Hg^0 removal efficiency was increased to 95.45%. Obviously, O_2 was favorable for Hg^0 removal and it was in accordance with previous studies [21,25]. The effect of H_2O and SO_2 were also investigated. In the presence of

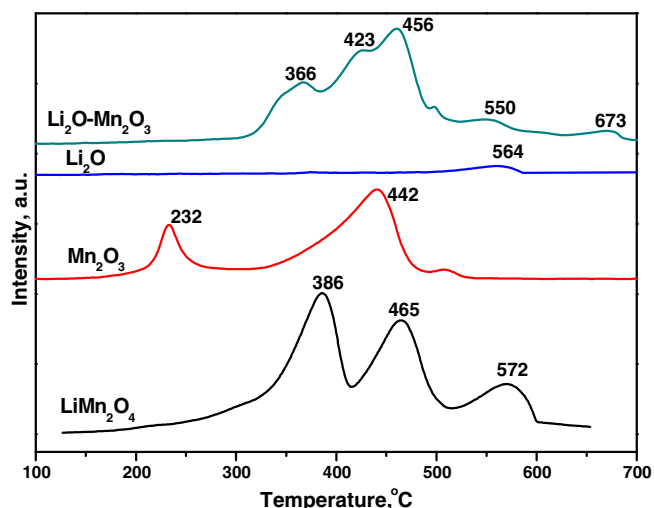


Fig. 8. H₂-TPR profiles of as-prepared samples.

500 ppm SO₂ + 4% O₂, the Hg⁰ removal efficiency decreased to 81.35%. The Mn based materials suffer from the poison of SO₂, the sulfate generated on the surface, resulted in the inactivation of Mn active sites. When the gas component was 4% H₂O + 4% O₂, the Hg⁰ removal efficiency was only 51.98%. H₂O also had higher poison effect on Hg⁰ removal compared to that of SO₂. With 500 ppm SO₂ + 4% H₂O + 4% O₂, the Hg⁰ removal efficiency decreased to only 20.72%. The co-existence of SO₂ and H₂O had a severe poisoning effect on Hg⁰ removal.

3.3. Hg⁰ removal mechanism over LiMn₂O₄ spinel oxide

As discussed above, LiMn₂O₄ presented excellent performance for Hg⁰ removal. The large surface area and the special spinel structure was beneficial for Hg⁰ removal. The Hg⁰ removal mechanism was generally ascribed to catalytic oxidation and chemical-adsorption process. The reducibility of the as-prepared samples was analyzed using H₂-temperature programmed reduction (H₂-TPR) (Fig. 8). For Mn₂O₃, two obvious peaks were detected at 232 and 442 °C, the peak at low temperature was ascribed to the reduction of surface oxygen and the peak at higher temperature were assigned to Mn³⁺ → Mn²⁺. [13] In the profile of Li₂O, there is a weak peak at high temperature of 564 °C and it can be ascribed to Li⁺ → Li⁰. For LiMn₂O₄, three characteristic peaks were presented, the peaks at 386 and 465 °C could ascribed to Mn⁴⁺ → Mn³⁺ and Mn³⁺ → Mn²⁺, respectively. As the temperature rising, a peak at 572 °C can be ascribed to Li⁺ → Li⁰. With the addition of Li ions in LiMn₂O₄, the valance of Mn was increased, resulted in the higher reducibility. For Li₂O–Mn₂O₃, it presented five character peaks in its profile, these peaks were ascribed to the reduction of Mn⁴⁺ → Mn³⁺, Mn³⁺ → Mn²⁺, Li²⁺ → Li⁰ and the interaction between Li and Mn ions (such as Li⁺ + Mn³⁺ ↔ Li⁰ + Mn⁴⁺ and Li⁺ + Mn²⁺ ↔ Li⁰ + Mn³⁺). Based on the H₂-TPR results, with the addition of Li, LiMn₂O₄ showed better reducibility than Mn₂O₃. The valance of Mn was increased based on the XPS results, and that the reduction of Mn⁴⁺ + e⁻ → Mn³⁺ offered an electrons for Hg⁰ oxidation. The active Li⁺ can acted as a good electron acceptor in the process which benefited catalytic oxidation.

After adsorption, the XPS spectra were presented in Fig. 9. For O 1s, the peaks at 531.2 and 530.0 eV were corresponded to O_{ads} and

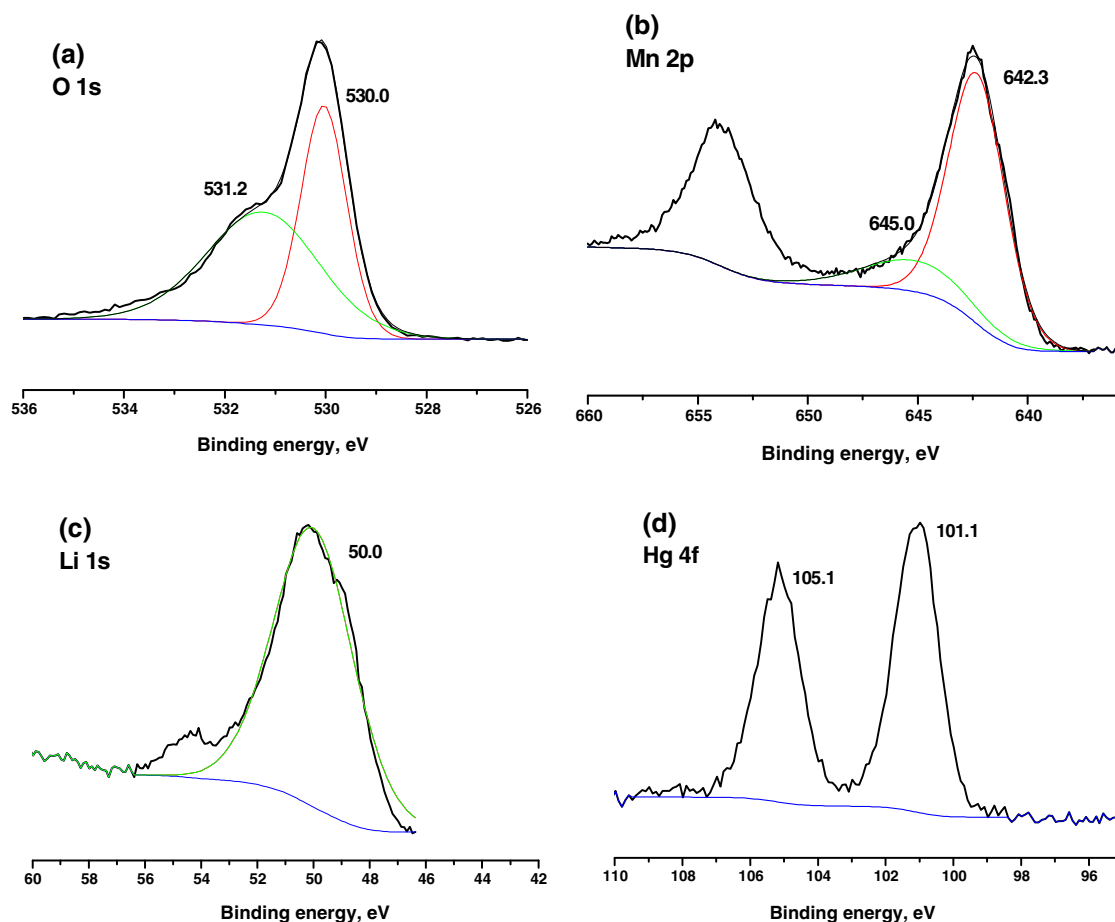


Fig. 9. XPS spectra of after adsorption LiMn₂O₄.

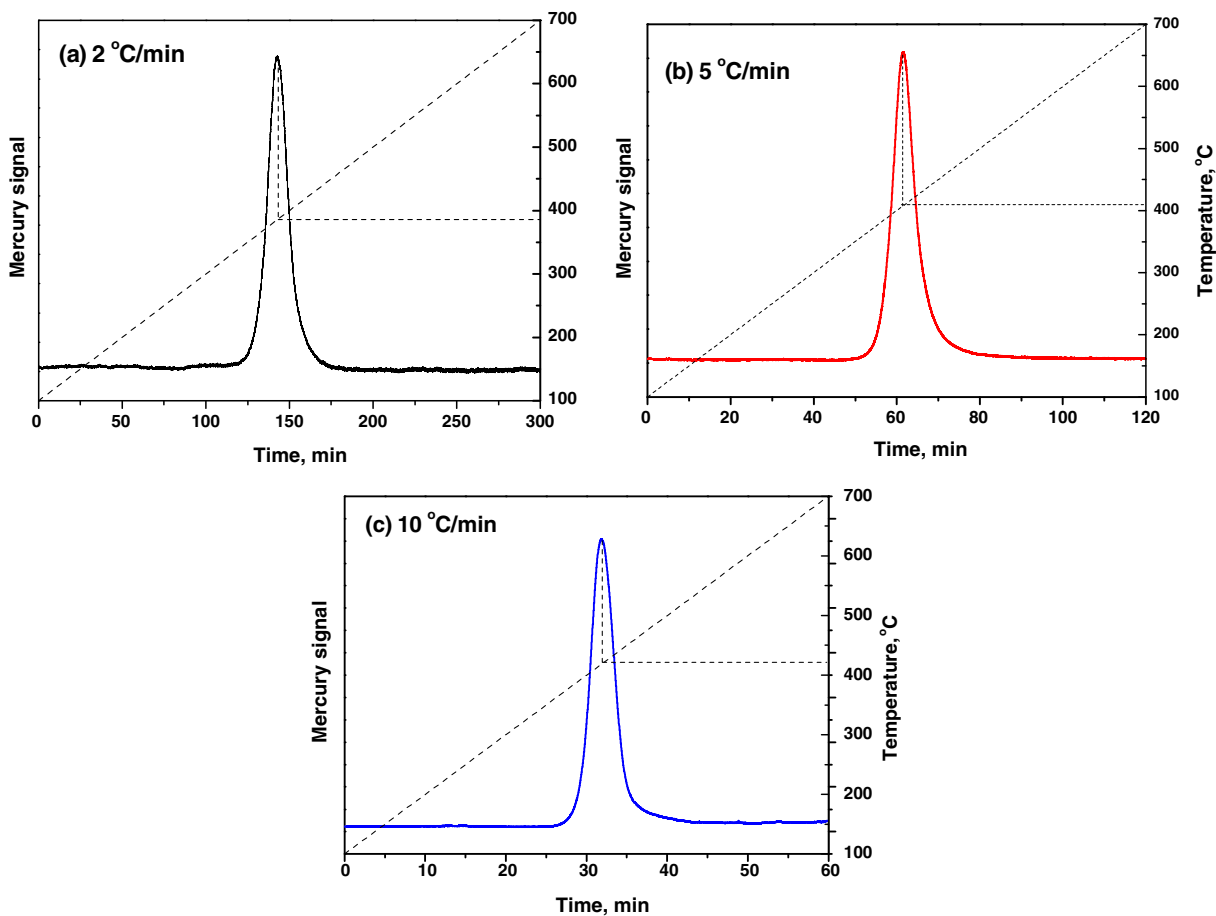
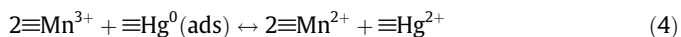
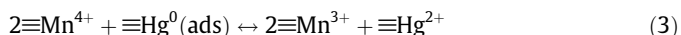


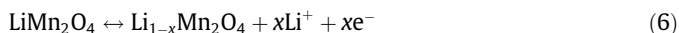
Fig. 10. Hg-TPD curves of LiMn_2O_4 at different heating rates.

O_{latt} . The ratio of $\text{O}_{\text{ads}}/\text{O}_{\text{latt}}$ was 55.32/44.68. The ratio was a slight increase compared to that of the fresh sample. This could be the reason that LiMn_2O_4 had oxygen adsorption performance. For the spectrum of Mn 2p, the peaks at 645.0 and 642.3 eV were corresponded to Mn^{4+} and Mn^{3+} , respectively. But the ratio of $\text{Mn}^{4+}/\text{Mn}^{3+}$ decreased from 21.88/78.12 to 18.86/81.14. Mn was the primary active sites for the catalytic oxidation. During the Hg^0 removal process, the high valance of Mn was reduced to the lower valance. In the spectrum of Li 1s, it had nearly no change. But on the surface of after adsorption sample, mercury was detected. In the spectrum of Hg 4f, the peaks at 105.1 and 101.1 eV can be ascribed to Hg–O bond. This indicated that the Hg^0 removal process was a chemical-adsorption process.

Gaseous Hg^0 was firstly adsorbed on the surface of Mn-based materials. And then the Hg^0 was oxidized to Hg^{2+} along with the reducing of Mn^{4+} to Mn^{3+} or Mn^{3+} to Mn^{2+} . The Hg^{2+} was finally chemical-adsorbed by surface oxygen. The processed is attributed to the Mars–Maessen mechanism [26], were described as follows:



During the Hg^0 removal process, the free Li^+ in the MnO_6 units was beneficial for electron transfer.



Base on H_2 -TPR results, the Li^+ in the λ - MnO_2 was beneficial for the interaction with higher valance of Mn. So Mn keep the higher valance state. MnO_2 had higher valance of Mn compared to that of Mn_2O_3 or the mixed $\text{Li}_2\text{O}-\text{Mn}_2\text{O}_3$ which was beneficial for the higher catalytic performance.

3.4. Regeneration test

As shown in Fig. 10, the property of regeneration was tested using the Hg-TPD method, and the activation energy for desorption was calculated. The results of the Hg-TPD curves under different rates of heating on LiMn_2O_4 are shown in Fig. 10. During the desorption process at each heating rate, one primary peak emerged on the Hg-TPD curves, suggesting that Hg–O bond the main specie on the LiMn_2O_4 surface. According to the results, mercury could be released at approximately 400 °C under pure N_2 conditions.

Based on the desorption data under different rates of heating, the desorption activation energy was calculated according to Eq. (7):

$$2\text{Ln}T_p - \text{Ln}\beta = \frac{E_d}{RT_p} - \text{Ln} \frac{E_d}{AR} \quad (7)$$

where T_p is the maximum value at a certain temperature (K), β is the heating rate (K/min), E_d is the desorption activation energy (kJ/mol), R is the gas constant, T is the temperature (K), and A is a pre-exponential factor. According to the Eq. (7), the desorption activation energies was 58.82 kJ/mol.

4. Conclusions

In summary, LiMn_2O_4 was synthesized the catalytic removal performance for Hg^0 was investigated. LiMn_2O_4 exhibited better performance compared to that of Mn_2O_3 and $\text{Li}_2\text{O}-\text{Mn}_2\text{O}_3$ mixed oxides. LiMn_2O_4 presented a spinel structure, with the addition of Li^+ ions, the surface area was enlarged. And the reducibility was enhanced. The Hg^0 removal mechanism can be described into two steps: (1) physical-adsorption: Hg^0 first adsorbed on LiMn_2O_4 , the larger surface area benefited physical-adsorption; (2) catalytic oxidation-adsorption: Hg^0 was oxidized by the reduction of Mn and adsorbed with oxygen. Furthermore, after adsorption, the mercury on LiMn_2O_4 surface can release using thermal decomposition method. The released mercury can be collected which protected from mercury secondary contamination.

Acknowledgments

This work was supported by the Major State Basic Research Development Program of China (973 Program, No. 2013CB430005), the National Natural Science Foundation of China (No. 51478261 and No. 51278294). Thanks for Shanghai Tongji Gao Tingyao Environmental Science and Technology Development Foundation.

References

- [1] C.-J. Lin, S.O. Pehkonen, The chemistry of atmospheric mercury: a review, *Atmos. Environ.* 33 (1999) 2067–2079.
- [2] J.H. Pavlish, E.A. Sondreal, M.D. Mann, E.S. Olson, K.C. Galbreath, D.L. Laudal, S. A. Benson, Status review of mercury control options for coal-fired power plants, *Fuel Process. Technol.* 82 (2003) 89–165.
- [3] A.A. Presto, E.J. Granite, Survey of catalysts for oxidation of mercury in flue gas, *Environ. Sci. Technol.* 40 (2006) 5601–5609.
- [4] J. Wilcox, E. Rupp, S.C. Ying, D.-H. Lim, A.S. Negreira, A. Kirchofer, F. Feng, K. Lee, Mercury adsorption and oxidation in coal combustion and gasification processes, *Int. J. Coal Geol.* 90 (2012) 4–20.
- [5] A.D. Jew, E.C. Rupp, D.L. Geatches, J.-E. Jung, G. Farfan, L. Bahet, J.C. Hower, G.E. Brown Jr, J. Wilcox, Mercury interaction with the fine fraction of coal-combustion fly ash in a simulated coal power plant flue gas stream, *Energy Fuels* 29 (2015) 6025–6038.
- [6] A. Suarez Negreira, J. Wilcox, Uncertainty analysis of the mercury oxidation over a standard SCR catalyst through a lab-scale kinetic study, *Energy Fuels* 29 (2014) 369–376.
- [7] J. Wo, M. Zhang, X. Cheng, X. Zhong, J. Xu, X. Xu, Hg²⁺ reduction and re-emission from simulated wet flue gas desulfurization liquors, *J. Hazard. Mater.* 172 (2009) 1106–1110.
- [8] J. He, C. Duan, M. Lei, X. Zhu, The secondary release of mercury in coal fly ash-based flue-gas mercury removal technology, *Environ. Technol.* 37 (2016) 28–38.
- [9] J. He, G.K. Reddy, S.W. Thiel, P.G. Smirniotis, N.G. Pinto, Ceria-modified manganese oxide/titania materials for removal of elemental and oxidized mercury from flue gas, *J. Phys. Chem. C* 115 (2011) 24300–24309.
- [10] H. Li, C.-Y. Wu, Y. Li, J. Zhang, Superior activity of $\text{MnOx}-\text{CeO}_2/\text{TiO}_2$ catalyst for catalytic oxidation of elemental mercury at low flue gas temperatures, *Appl. Catal. B* 111 (2012) 381–388.
- [11] H. Xu, J. Xie, Y. Ma, Z. Qu, S. Zhao, W. Chen, W. Huang, N. Yan, The cooperation of Fe Sn in a MnOx complex sorbent used for capturing elemental mercury, *Fuel* 140 (2015) 803–809.
- [12] S. Yang, Y. Guo, N. Yan, D. Wu, H. He, J. Xie, Z. Qu, J. Jia, Remarkable effect of the incorporation of titanium on the catalytic activity and SO_2 poisoning resistance of magnetic Mn–Fe spinel for elemental mercury capture, *Appl. Catal. B* 101 (2011) 698–708.
- [13] H. Xu, Z. Qu, S. Zhao, J. Mei, F. Quan, N. Yan, Different crystal-forms of one-dimensional MnO_2 nanomaterials for the catalytic oxidation and adsorption of elemental mercury, *J. Hazard. Mater.* 299 (2015) 86–93.
- [14] J. Chen, M. Shen, X. Wang, J. Wang, Y. Su, Z. Zhao, Catalytic performance of NO oxidation over LaMeO_3 (Me = Mn, Fe, Co) perovskite prepared by the sol–gel method, *Catal. Commun.* 37 (2013) 105–108.
- [15] J. Zhu, H. Li, L. Zhong, P. Xiao, X. Xu, X. Yang, Z. Zhao, J. Li, ChemInform abstract: perovskite oxides: preparation, characterizations, and applications in heterogeneous catalysis, *ChemInform* 45 (2014).
- [16] H. Xu, Z. Qu, C. Zong, F. Quan, J. Mei, N. Yan, Catalytic oxidation and adsorption of Hg⁰ over low-temperature NH₃-SCR LaMnO_3 perovskite oxide from flue gas, *Appl. Catal. B: Environ.* (2015).
- [17] Z. Zhou, X. Liu, B. Zhao, H. Shao, Y. Xu, M. Xu, Elemental mercury oxidation over manganese-based perovskite-type catalyst at low temperature, *Chem. Eng. J.* 288 (2016) 701–710.
- [18] Y. Wang, Y. Wang, D. Jia, Z. Peng, Y. Xia, G. Zheng, All-nanowire based Li-ion full cells using homologous Mn_2O_3 and LiMn_2O_4 , *Nano Lett.* 14 (2014) 1080–1084.
- [19] D.M. Robinson, Y.B. Go, M. Mui, G. Gardner, Z. Zhang, D. Mastrogianni, E. Garfunkel, J. Li, M. Greenblatt, G.C. Dismukes, Photochemical water oxidation by crystalline polymorphs of manganese oxides: structural requirements for catalysis, *J. Am. Chem. Soc.* 135 (2013) 3494–3501.
- [20] D.M. Robinson, Y.B. Go, M. Greenblatt, G.C. Dismukes, Water oxidation by λ - MnO_2 : catalysis by the cubical Mn_4O_4 subcluster obtained by delithiation of spinel LiMn_2O_4 , *J. Am. Chem. Soc.* 132 (2010) 11467–11469.
- [21] H.M. Xu, Z. Qu, C.X. Zong, W.J. Huang, F.Q. Quan, N.Q. Yan, MnOx/graphene for the catalytic oxidation and adsorption of elemental mercury, *Environ. Sci. Technol.* 49 (2015) 6823–6830.
- [22] J. Cho, T.J. Kim, J.K. Yong, B. Park, Complete blocking of Mn³⁺ ion dissolution from a LiMn_2O_4 spinel intercalation compound by Co_3O_4 coating, *Chem. Commun.* 12 (2001) 1074–1075.
- [23] C.V. Ramana, R.J. Smith, O.M. Hussain, M. Massot, C.M. Julien, Surface analysis of pulsed laser-deposited V_2O_5 thin films and their lithium intercalated products studied by Raman spectroscopy, *Surf. Interface Anal.* 37 (2005) 406–411.
- [24] S.J. Hwang, D.H. Park, J.H. Choy, G. Campet, Effect of chromium substitution on the lattice vibration of spinel lithium manganate: a new interpretation of the Raman spectrum of LiMn_2O_4 , *J. Phys. Chem. B* 108 (2004) 12713–12717.
- [25] J. Li, N. Yan, Z. Qu, S. Qiao, S. Yang, Y. Guo, P. Liu, J. Jia, Catalytic oxidation of elemental mercury over the modified catalyst Mn/ α - Al_2O_3 at lower temperatures, *Environ. Sci. Technol.* 44 (2009) 426–431.
- [26] S. Yang, Y. Guo, N. Yan, D. Wu, H. He, J. Xie, Z. Qu, C. Yang, J. Jia, A novel multi-functional magnetic Fe–Ti–V spinel catalyst for elemental mercury capture and callback from flue gas, *Chem. Commun.* 46 (2010) 8377–8379.